

## Article

# Investigation of Corrosion Properties and Composition of the Surface Formed on AISI 321 Stainless Steel by Ion Implantation

Tamara I. Dorofeeva, Marina V. Fedorischeva \* , Tatiana A. Gubaidulina, Oleg V. Sergeev, Alfred R. Sungatulin and Viktor P. Sergeev

Laboratory of Nanotechnology and Materials Science of Coatings, Institute of Strength Physics and Materials Science SB RAS, 634055 Tomsk, Russia; dorofeeva@ispms.ru (T.I.D.); goub2002@mail.ru (T.A.G.); tehnovak@sibnet.ru (O.V.S.); alfred\_1972@mail.ru (A.R.S.); vs@ispms.ru (V.P.S.)

\* Correspondence: fed\_mv@mail.ru; Tel.: +7-962-776-3406

**Abstract:** In this work, the corrosion resistance of AISI 321 stainless steel is increased through the two-stage implantation of oxygen ions and of both aluminum and boron ions together. During ion implantation, a modified layer with a thickness of about 200 nm is formed, which affects the properties of material. The increase in corrosion resistance is confirmed by prolonged acid corrosion tests at pH 3.5 and by accelerated electrochemical tests using a potentiostat. The corrosion rate of the implanted sample is  $0.708 \mu\text{A}/\text{cm}^2$ , in contrast to the non-implanted sample ( $1.26 \mu\text{A}/\text{cm}^2$ ). The modified surface layer is examined using X-ray photoelectron spectroscopy (XPS), secondary-ion mass spectrometry (SIMS), and transmission electron microscopy (TEM). Aluminum and boron are implanted to a depth of more than 250 nm. It is found that the modified surface of the stainless steel substrate contains oxides of implanted ions ( $\text{Al}_2\text{O}_3$ ) and oxides of substrate ions ( $\text{Cr}_2\text{O}_3$  and  $\text{NiCr}_2\text{O}_4$ ).

**Keywords:** ion beam implantation; stainless steel; corrosion resistance; implanted ions of O, B, and Al



**Citation:** Dorofeeva, T.I.; Fedorischeva, M.V.; Gubaidulina, T.A.; Sergeev, O.V.; Sungatulin, A.R.; Sergeev, V.P. Investigation of Corrosion Properties and Composition of the Surface Formed on AISI 321 Stainless Steel by Ion Implantation. *Metals* **2023**, *13*, 1468. <https://doi.org/10.3390/met13081468>

Academic Editors: Belén Díaz Fernández, Jianqiang Wang and Branimir N. Grgur

Received: 30 June 2023

Revised: 2 August 2023

Accepted: 8 August 2023

Published: 15 August 2023



**Copyright:** © 2023 by the authors. Licensee MDPI, Basel, Switzerland. This article is an open access article distributed under the terms and conditions of the Creative Commons Attribution (CC BY) license (<https://creativecommons.org/licenses/by/4.0/>).

## 1. Introduction

Stainless steel is in high demand in the production of equipment for the petrochemical, transport, engineering, processing, and food industries. Chromium-nickel stainless steel occupies a leading position among special structural materials due to its good resistance to aggressive media. However, continuous sour service of the steel, combined with mechanical stress or temperature, sharply reduces its resistance to corrosion. Various methods of surface treatment are used to increase the corrosion resistance of stainless steel.

The most common methods of protection of steel products are in-process alloying, the introduction of corrosion inhibitors, cathodic protection, and the formation of an inert layer that insulates the substrate material and prevents it from dissolution by applying special pastes, gels, varnishes, paints or other resistant materials [1,2]. These layers formed on the surface to protect against corrosion are called protective coatings. They not only prevent corrosion, but also provide additional physical and chemical properties (wear resistance, electrical conductivity, etc.). The necessary properties of all types of coatings are high adhesion, continuity, and resistance to aggressive media. A protective layer can be formed on the surface by various methods: electrochemical [3,4] and chemical ones [5,6], thermal diffusion [7,8], laser cladding [9,10], magnetron sputtering [11–15], plasma deposition [16], ion implantation [17–21], etc.

Ion implantation has been known for a very long time [22–24] and is still one of the ways to modify materials [25]. Ion implantation improves the physical and mechanical properties of the material surface (hardness, heat resistance, wear resistance, fatigue strength, corrosion resistance, etc.) [20,26–30]. The main advantages of ion implantation include the absence of adhesion problems [31] (since ions are implanted into the material

at an energy of about 106 eV) and no influence on the geometric dimensions of workpieces, which is relevant for cutting tools or threaded joints [32]. Ion implantation is especially effective for the corrosion protection of products made of high-strength materials, whose strength properties are worsened by the standard thermochemical treatment.

The choice of materials for ion implantation is the most important factor. This treatment should improve the physical and chemical properties of the resulting material. It is known that boron increases the hardness and wear resistance of materials [33–36]. The boriding of steel to increase its corrosion resistance is carried out in various ways, and the thickness of the resulting layer often exceeds 20  $\mu\text{m}$  [34,37–40]. The introduction of even a small amount of boron reduces the rate at which carbides coarsen. Thus, in stabilizing the steel microstructure [41], boron prevents the intergranular corrosion characteristics of stainless steels [42]. Boron implantations lead to a significant reduction in the oxidation rate of a substrate [43].

The authors [44] have shown that the fracture toughness increased and scratch test results revealed an improvement in the tribological behavior of the oxygen implanted surface compared to the un-implanted substrate, and that oxygen ion implantation slightly improved high-temperature oxidation resistance. The ion implantation of  $\text{O}^+$  ions gives optimal results in terms of a reduction in localized and general corrosion, the surface is demonstrated to undergo intense oxidation to a depth of  $>20$  nm, which contributes to the formation of corrosion-resistant mixtures [45]. Oxides of the substrate material are formed during the implantation of oxygen ions [46]. The formation of oxide layers and various adsorbed oxygen species contributes to the transition of the surface to a passive state [47].

Aluminum implanted into the material forms aluminum oxide,  $\text{Al}_2\text{O}_3$ , on the surface, which not only promotes corrosion resistance in aggressive media [48–50] but also increases thermal stability [51,52]. Al implantation can enhance the wear resistance of alloy. The dramatically improved corrosion resistance is considered to result from the formation of a large amount of  $\text{Al}_2\text{O}_3$  [53]. In addition, aluminum oxide formed in surface layers has no interfaces with the substrate and excludes adhesion problems [54].

Aluminum films were doped with boron to increase their hardness [55]. It was shown [56,57] that the Al–B-based coatings have increased hardness and wear resistance.

The present paper deals with the combined effect of aluminum, boron, and oxygen implantation on the corrosion resistance of the stainless steel without changing the geometric dimensions. The effectiveness of ion implantation against corrosion was established in references [17,20,45], but the chemical changes occurring in surface layers during implantation and that increase corrosion resistance are poorly understood.

The aim of the present work is to study the technological features of the implantation process associated with the sequence of ion implantation on the physical and chemical structure of the implanted surface layers and the corrosion behavior of the material.

## 2. Materials and Methods

The material chosen for investigation is sheet stainless steel 12Cr18Ni10Ti (analogous to AISI 321) of the composition 1.12 wt.% Si, 9.69 wt.% Ti, 0.65 wt.% Mn, 16.99 wt.% Cr, 9.57 wt.% Ni, and 61.9 wt.% Fe, which has the thickness 1 mm. Specimens measuring 10 mm  $\times$  10 mm are cut from the steel sheets. Surface roughness is analyzed using an Alpha-Step IQ Surface Profiler (HRP 350 series, KLA-Tencor, Milpitas, CA, USA).

Before implantation, the specimens are mechanically ground and mirror-polished to achieve the average roughness  $R_a = 0.10 \div 0.01$ .

Ion implantation is performed using a UVN-05MD KVANT vacuum unit (Elektronvak Ltd., Tomsk, Russia) equipped with the Diana and Dionis implanters. Dionis is used for implantation of gas ions. Diana is used for implantation of metal ions with the use of an appropriate target. Ions used for implantation are  $\text{Al}^+$ ,  $\text{B}^+$ , and  $\text{O}^+$ . Oxygen implantation is carried out using the Dionis implanter. Aluminum and boron are implanted simultaneously using the mosaic target in an inert gas atmosphere in the Diana implanter. The target for aluminum and boron implantation is composed of an aluminum-based alloy (99 at.%

Al), with cylindrical pins of 96.999 at.% pure boron (Russia). The ion implantation is performed in two steps. Oxygen implantation is followed by the simultaneous implantation of aluminum and boron. The implantation modes used at these two stages are presented in Table 1.

**Table 1.** Modes of the O/Al-B ion implantation on the steel surface.

Mode Parameters	Stage I	Stage II
Installation	Dionis	Diana
Implanted ions	O <sup>+</sup>	Al <sup>+</sup> B <sup>+</sup>
Gas	O <sub>2</sub>	N <sub>2</sub>
Target	-	Al-B
Residual pressure, A	1 × 10 <sup>-8</sup>	1 × 10 <sup>-8</sup>
Gas pressure, A	1 × 10 <sup>-6</sup>	1 × 10 <sup>-7</sup>
Emission current, mA	100	-
Beam current, mA	15	300
Accelerating voltage, kV	10	40 ÷ 80
Implantation dose, ion/cm <sup>2</sup>	1 × 10 <sup>18</sup>	4 × 10 <sup>17</sup>

Corrosion resistance is tested in a CSS-2 salt spray chamber (HTCUAI, Bashkortostan, Ufa, Russia) in an acidic medium for a month with the periodic measurement of the specimen weight. The corrosion current is estimated from the Tafel current–voltage curves obtained using a P-45X potentiostat (Electrochemical Instruments, Chernogolovka, Russia). Polarization measurements are carried out at room temperature (25 °C) under static conditions (without aeration) using the three-electrode system involving an Ag/AgCl electrode (4.2 M). The sea salt solution (3.5 wt.% NaCl) is chosen as the corrosive medium. The measurements are performed in the potentiodynamic mode at the linear potential sweep rate 1 mV/s; the potential varies from –800 to 800 mV. Before measurements, the specimen is held in the solution for at least 30 min to reach the equilibrium potential.

Surface analysis is carried out by X-ray photoelectron spectroscopy on a Thermo Electron Escalab 250 Spectrometer (Thermo Scientific, Waltham, MA, USA) using the monochromatic AlK $\alpha$  X-ray source (1486.6 eV). The base pressure in the analytical chamber is maintained at 10<sup>-9</sup> Mbar. The spectrometer is calibrated using the Au 4f 7/2 peak at 84.1 eV. The X-ray beam angle is 90°, and the X-ray spot size is 500  $\mu$ m. Survey spectra are recorded with the X-ray energy 100 eV and step 1 eV. High-resolution C1s, O1s, Fe2p, Cr2p, Ni2p, Al3d, and B1s spectra are recorded with the X-ray energy 20 eV and step 0.1 eV. Spectral-line shape fitting is performed using the Advantage software (Version 5.938) by the iterative Shirley background subtraction procedure.

The elemental composition of the implanted layer is determined by secondary-ion mass spectrometry using an MS-7201M mass spectrometer (Selmi, Sumy, Ukraine) with the sensitivity threshold up to 10<sup>14</sup> at/cm<sup>3</sup>. The SIMS technique involves continuous bombardment of the specimen surface with a focused high-energy beam of primary ions with subsequent collection and analysis of ejected secondary ions. The mass/charge ratios of these secondary ions are measured with the mass spectrometer to determine the elemental, isotopic or molecular composition of the surface layer with the thickness 1–2 nm. Sputtering occurs at the flow of argon ions with the energy of up to 5 keV at the current of primary ions 40  $\mu$ A/cm<sup>2</sup>. The probing beam diameter is 1 mm, and the depth analysis rate is up to 5 nm/min.

The modified layer thickness is estimated on cross-sectional thin foils with a JEM-2100 electron microscope (JEOL, Tokyo, Japan) in the bright-field and dark-field modes. Cross-sectional thin foils are prepared by mechanical thinning followed by Ar ion-beam milling using an EM 09100IS ion slicer (JEOL, Tokyo, Japan).

Scanning electron microscopy is used to study the surface morphology of specimens before and after corrosion tests using a LEO EVO 50 microscope (Zeiss, Oberhochen, Germany).

### 3. Results and Discussion

#### 3.1. SIMS Analysis

Aluminum and boron ion implantation is carried out at the implantation dose  $1 \times 10^{17}$  ion/cm<sup>2</sup> and the accelerating voltage 80 kV, which is sufficient for Al and B ions to enter the material surface. The aluminum and boron ion implantation is followed by the implantation of oxygen ions into the stainless steel. It was experimentally found that the implantation dose  $1 \times 10^{18}$  ion/cm<sup>2</sup> gives a sufficient oxygen concentration of 30%. Figure 1 shows the results of secondary-ion mass spectrometry.

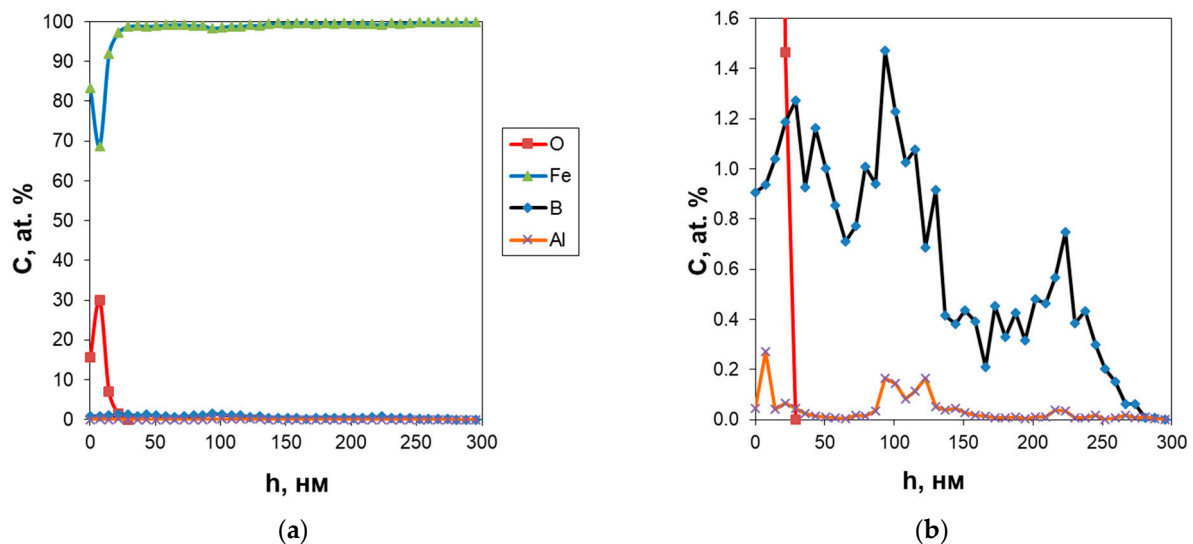


Figure 1. Depth profiles of O and Fe (a) and O, Fe, B, and Al (b) after ion implantation.

The level of damage and the local concentration of O in the 50 nm thick layer are controlled by the ion energy. The oxygen ion implantation is performed using low-energy ions. Therefore, the fluence chosen for the oxygen implantation is  $10^{18}$  ion/cm<sup>2</sup>. The SIMS results suggest that the ion energy 10 keV at the fluence  $10^{18}$  ions/cm<sup>2</sup> would result in the localization of implanted O ions in the 50 nm thick layer, which are confined to the 200 nm thick layer.

When oxygen is implanted in the second stage, the thickness of the aluminum and boron layer decreases significantly, as does their concentration in this layer (results of experimental studies). Oxygen creates a barrier layer to prevent boron and aluminum from penetrating far into the material, concentrating aluminum and boron in the surface layers [58]. If boron and aluminum are implanted at the first step and oxygen at the second step, the depth of ion implantation decreases to 60 nm according to the SIMS results. Figure 1b also shows the depth profiles of O, Al, and B plotted using the SIMS images. The concentration of implanted O, B, and Al ions decreases with depth in the 270 nm thick layer. From the profiles, it can be seen that the coating has a bilayer structure. Oxygen is implanted to a depth of no more than 25 nm, while aluminum and boron are implanted to a depth of more than 200 nm. The O modulation signal is greater than the Al and B signals: the O signal exceeds the Al and B signals by 30 times in the 10 nm thick bilayer.

#### 3.2. EDX Spectra and TEM Analysis

In the initial state, AISI 321 steel is composed of rather coarse austenite grains with titanium carbide inclusions. Cross-sectional transmission electron microscopy of the implanted steel reveals a significant refinement of the steel structure after the treatment with oxygen, aluminum, and boron ions. This is evidenced by the main 111 and 200 reflections of the  $\gamma$ -phase, forming rings. A modified layer with a thickness of about 20 nm is also visible. The electron microscopic images of the cross-sectional foils of the implanted specimen are presented in Figure 2a,d, which show a modified layer with a thickness varying from 150 to

250 nm and an oxide layer of about 5 nm resulting from the exposure of the specimen to air. A similar 5 nm thick layer was found on the surface of the non-implanted specimens [59,60]. Oxides probably form on low-angle boundaries and dislocation. The XPS of the implanted sample shows the presence of Fe in Fe<sup>0</sup>, Fe<sup>2+</sup>, and Fe<sup>3+</sup> [61]. The oxides formed on the surface are Al<sub>2</sub>O<sub>3</sub>, Fe<sub>3</sub>O<sub>4</sub>, Fe<sub>2</sub>O<sub>3</sub>, and FeCr<sub>2</sub>O<sub>4</sub>. This is evidenced by the microdiffraction patterns and dark-field images using the corresponding reflections.

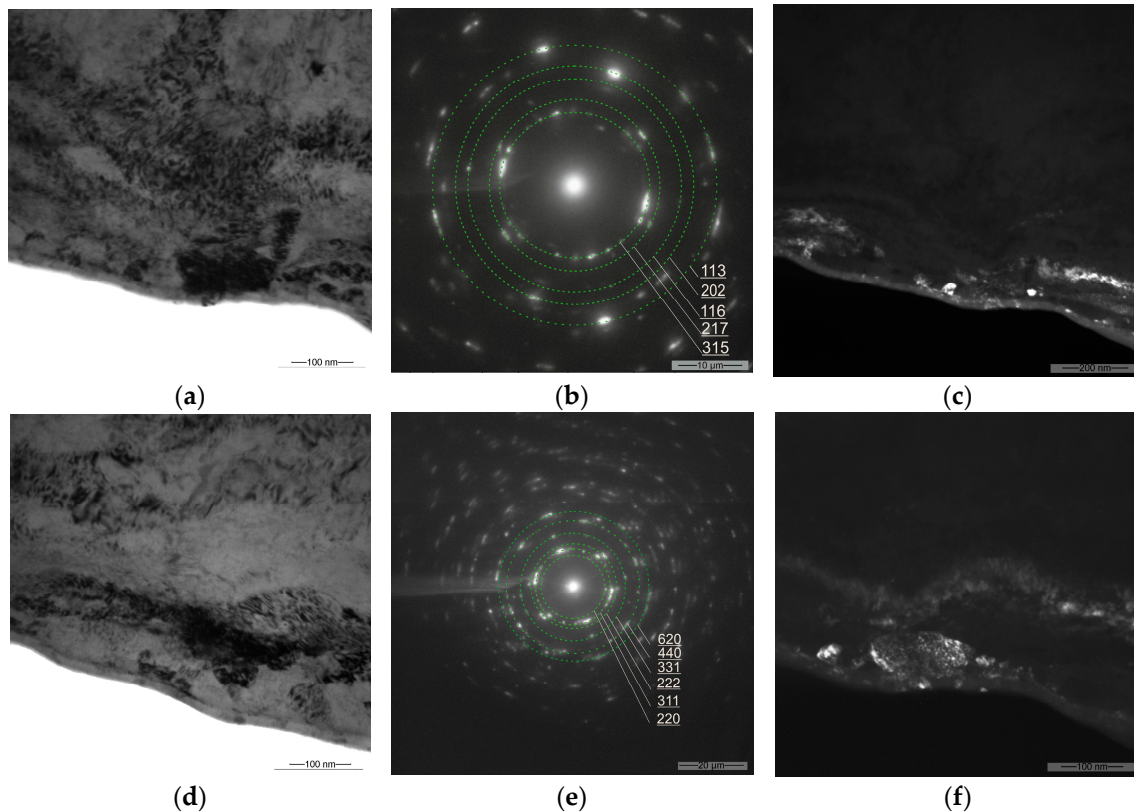


**Figure 2.** TEM images of the steel after oxygen, aluminum, and boron ion implantation: bright-field images (a,d); microdiffraction patterns (b,e); dark-field images (c,f) in the (202) Al<sub>2</sub>O<sub>3</sub> (c) and (311) FeCr<sub>2</sub>O<sub>4</sub>/NiCr<sub>2</sub>O<sub>4</sub> reflections (f).

The size of the structural elements visible in the dark-field image ranges from several to 100 nm. Figure 2 shows the electron microscopic images of the cross section of the implanted steel, the microdiffraction patterns, and the dark-field images taken using the 202 reflection of Al<sub>2</sub>O<sub>3</sub> (rhombohedral lattice R-3c with  $a = 4.62 \text{ \AA}$  and  $c = 12.57 \text{ \AA}$ ) and the (311) reflection of FeCr<sub>2</sub>O<sub>4</sub> (cubic lattice Fd3m with  $a = 8.348 \text{ \AA}$ ) and NiCr<sub>2</sub>O<sub>4</sub> (cubic lattice with  $a = 8.32 \text{ \AA}$ ).

Iron, aluminum, and chromium oxides are also found across the cross section, which penetrate to a depth of up to 1000 nm. This is evidenced by the depth profiles of the elements in the implanted steel.

Figure 3 shows the depth profiles for non-implanted and O/Al-B ion implanted specimens of AISI 321 steel. It can be seen that the non-implanted steel has a uniform depth distribution of elements, which corresponds to the initial composition. In the implanted steel, the oxygen concentration is about 10 at.%, which is two times higher than in the initial state. The concentration of aluminum is about 5 at.% at the depth 100 nm and further decreases to almost zero: a small amount of aluminum is found at the depth of 400 nm from the surface. It can be clearly seen that the concentration of oxygen in the implanted specimen is retained up to a depth of 600 nm. This may be the reason for the formation of a larger amount of oxides at a greater depth during ion treatment, which provides corrosion protection.

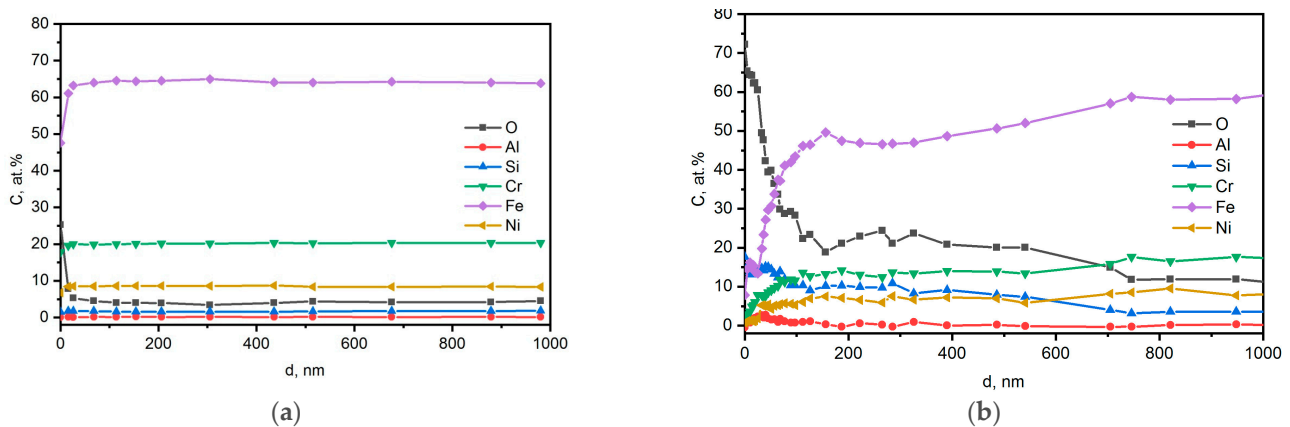


**Figure 3.** Depth profiles of elements in AISI 321 steel: in the initial state (a) and after O/Al-B ion implantation (b).

### 3.3. Corrosion Properties

The corrosion resistance of the non-implanted and implanted steel in aggressive media is estimated by prolonged corrosion tests in the salt spray chamber (5 wt.% NaCl solution with acetic acid, pH = 3). The corrosion tests of the initial specimens result in surface corrosion damage with the weight loss (Figure 4a). The weight of the implanted specimen is practically unchanged. In this case, the weight loss appears at the testing time 480 h. Consequently, it is recommended to avoid testing without corrosion protection, especially in prolonged tests.

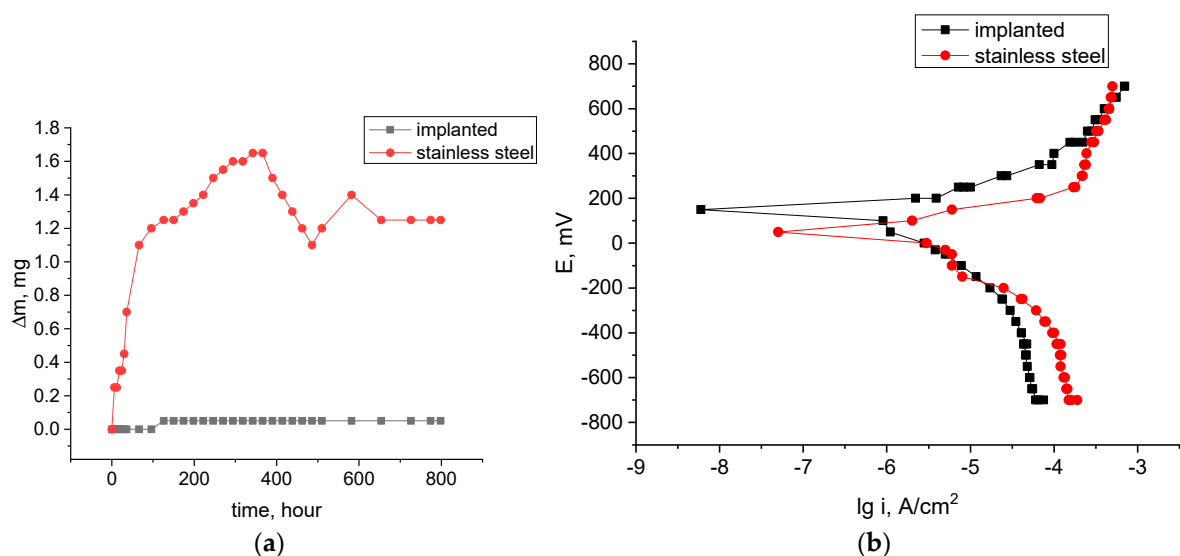


**Figure 4.** Corrosion behavior for the non-implanted and implanted specimens in the salt spray chamber at room temperature (a); potentiodynamic polarization curves of the non-implanted and implanted specimens (b).

The electrochemical behavior is evaluated in the 3.5 wt.% NaCl solution. To stabilize the ion exchange between the specimen and the electrolyte, the specimen is immersed in the 3.5 wt.% NaCl solution for 15 min before electrochemical measurements. The potential is swept at the rate of 1 mV/s for potentiodynamic polarization measurements (Figure 4b).

The corrosion potentials before and after implantation are 50 and 150 mV, respectively (Figure 4b). The latter moves to a more positive position, which indicates an improvement in the structural stability of the ion-implanted stainless steel. During corrosion testing, the corrosion current density decreases from 1.26 to 0.708  $\mu\text{A}/\text{cm}^2$ . The corrosion potential of the implanted specimen is high in comparison to the corrosion potential of the

initial stainless steel (50 mV). The corrosion potential of the implanted specimen shifts towards increasing potential, and its activation and reactivation current densities increase significantly.

Therefore, ion implantation can effectively improve the corrosion resistance of metal materials, which is mainly related to its structural stability above the corrosion initiation point.

It is found that implantation increases the corrosion potential (Table 2) and decreases the corrosion current. This is explained by the formation of a modified layer with a greater corrosion resistance. The improvement in corrosion resistance is always accompanied by the shift of the potential towards its increase and a decrease in the corrosion current density which determines the corrosion rate.

**Table 2.** Electrochemical parameters calculated from the polarization dependences.

Specimen	$E$ , mV	$lg i_{cor}$ , A/cm <sup>2</sup>	$i_{cor} \times 10^{-6}$ , A/cm <sup>2</sup>	$I_{cor}$ , A
Initial	52 ± 3	−5.9 ± 0.2	1.26	1.26 × 10 <sup>−6</sup>
O/Al-B ion-implanted	151 ± 6	−6.1 ± 0.2	0.71	0.71 × 10 <sup>−6</sup>

Implantation does not form a coating layer but modifies near-surface layers. During implantation, oxygen penetrates into the steel and oxidizes metallic chromium and other alloy elements with the formation of corrosion-resistant oxides Cr<sub>2</sub>O<sub>3</sub>, NiO, and spinels NiCr<sub>2</sub>O<sub>4</sub> [62–64], which protect the material from corrosion.

Morphological studies of the implanted surfaces after corrosion tests (Figure 5) reveal no changes (dark inclusions correspond to titanium nitride according to the elemental analysis data).

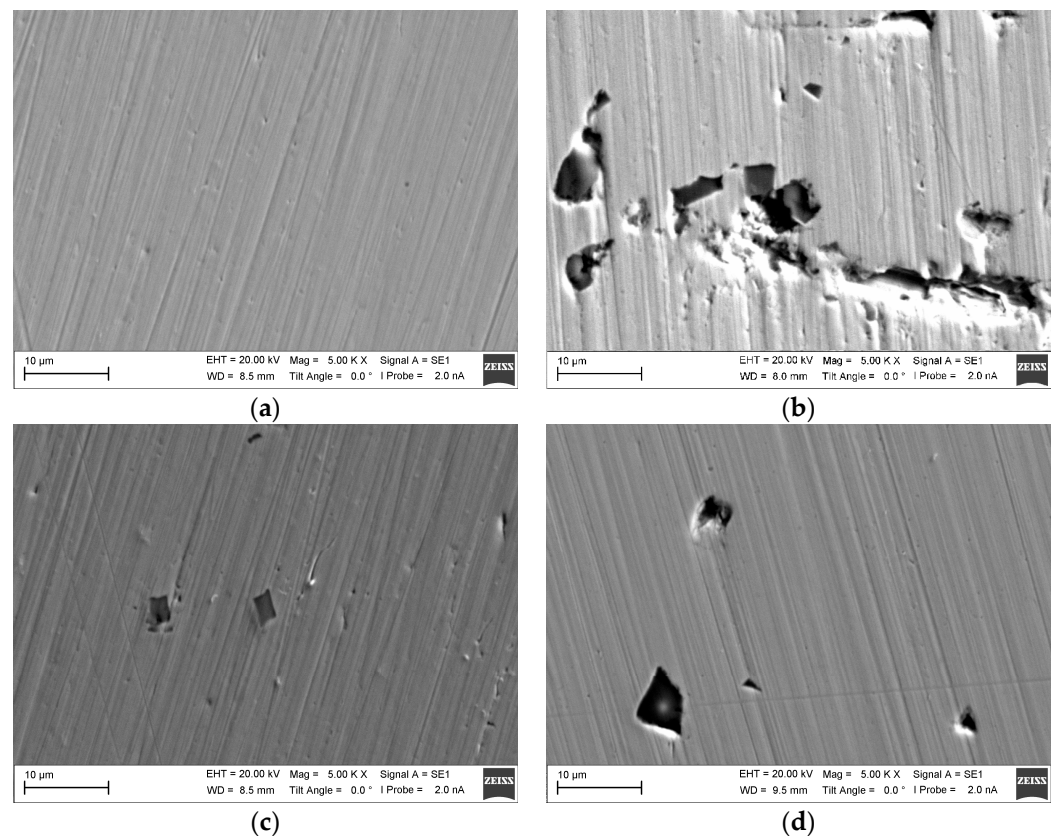


**Figure 5.** SEM images (LEO EVO-50XVP) of the non-implanted (a,b) and implanted (c,d) stainless steel specimens before (left) and after electrochemical corrosion tests (right).

### 3.4. XPS Analysis

The TEM data are in good agreement with the XPS results, which bear witness to changes in the concentration and chemical state of elements in the surface layers of the ion-implanted material.

The general spectrum recorded for the surface film after implantation (Figure 6) shows that the main elements found on the surface are iron, chromium, nickel, oxygen, and carbon. Small concentrations of aluminum and boron are also found. Boron, which was previously identified using the SIMS method, is found to be located at a depth of no more than 50 nm from the surface (Figure 6). The analysis of the aluminum spectra is complicated by the aluminum and nickel peak overlap. The presence of aluminum in the steel was confirmed by electron microprobe analysis. The presence of carbon (Figure 6, the curve at the depth of 0 nm) is due to the presence of carbon in the initial steel in the form of TiC, including due to surface contamination.

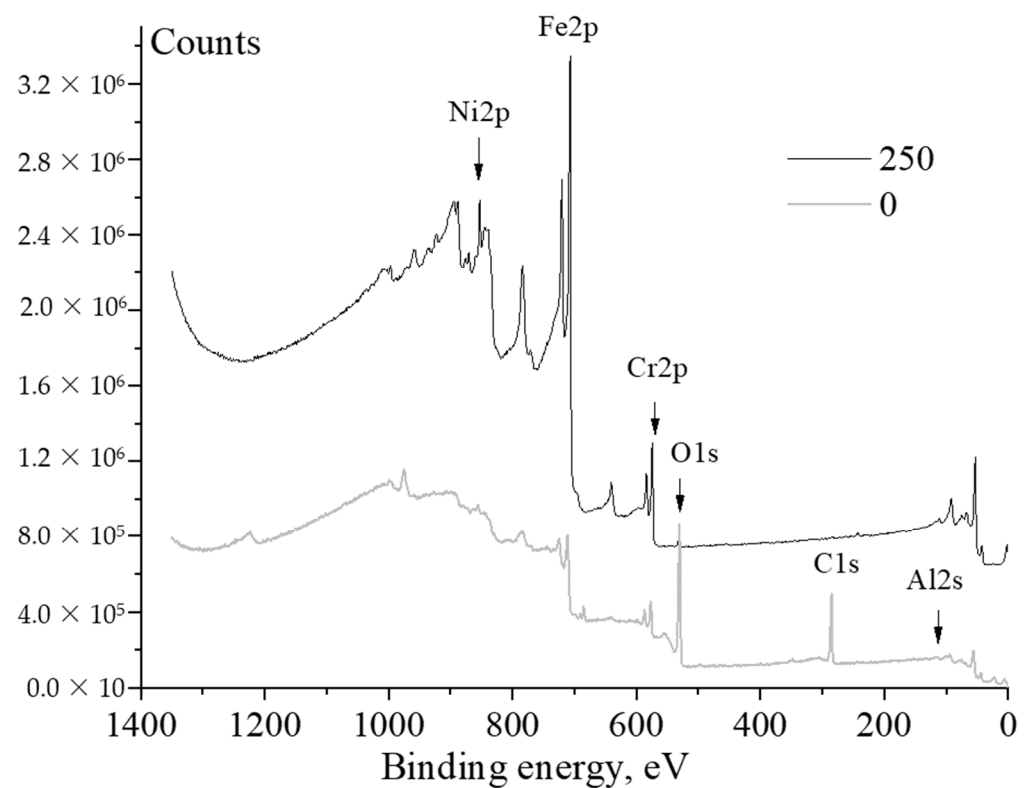


**Figure 6.** XPS spectra recorded for the implanted stainless steel on the surface (0 nm) and at the depth of 250 nm.

A high oxygen concentration in near-surface layers indicates that the alloy elements are mainly in the oxidized state up to a depth of 50 nm. Then, this ratio changes and, at a depth of 250 nm, the metallic state begins to prevail over the oxidized one. The quantitative content of metallic iron and metallic chromium is much higher than that of the oxidized metals at the depth of 250 nm, which can clearly be seen in Figure 6.

Separate spectral lines for each element show that ion implantation decreases the concentration of Fe and Cr on the surface, and that these elements are mainly in the oxidized state (Figure 7). Moreover, the depth of distribution of the Fe and Cr oxides reaches about 300 nm due to the deep penetration of oxygen ions during the treatment with O/Al-B ions.

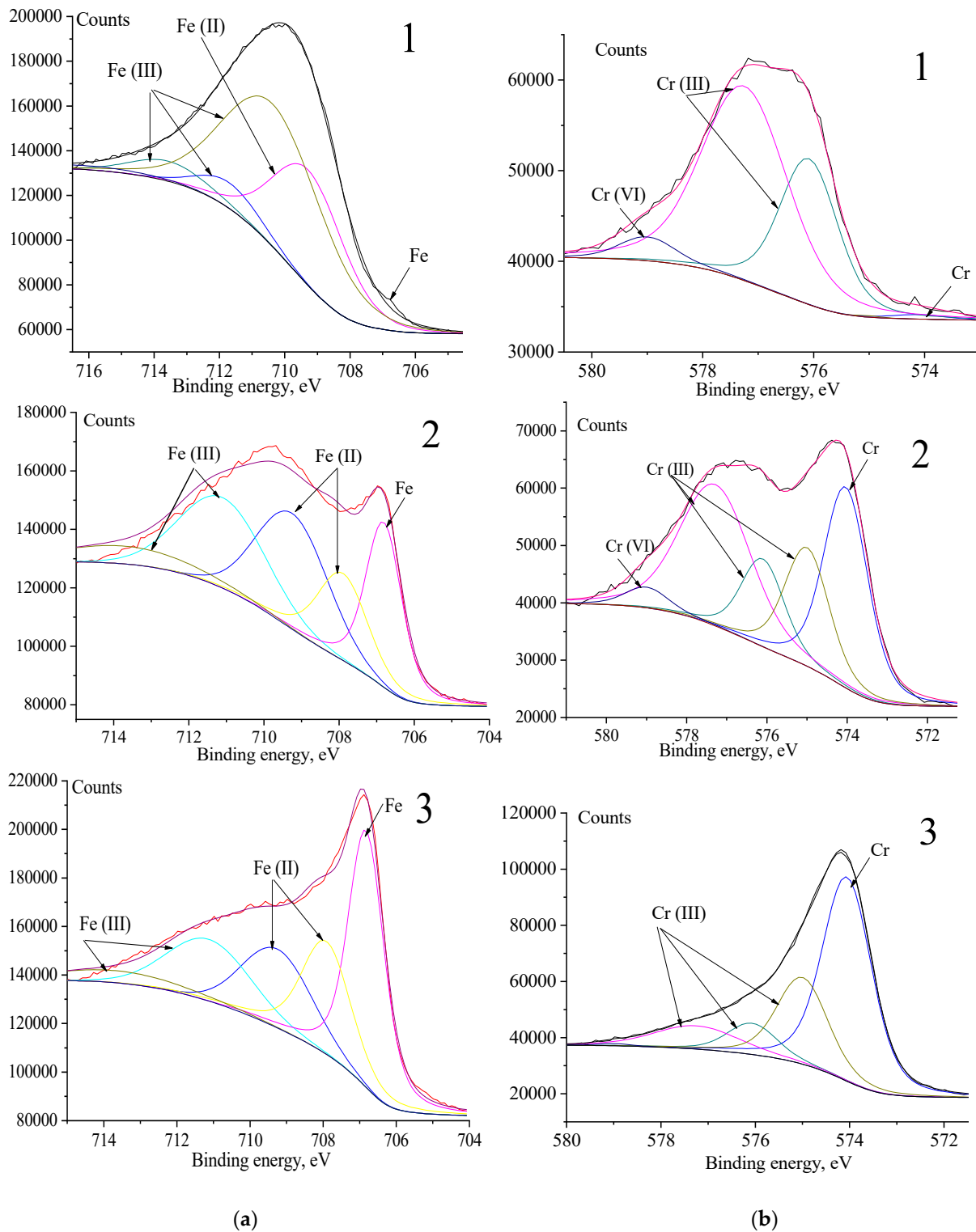


**Figure 7.** XPS spectra of iron (a) and chromium (b) recorded at the depths of 0 (1), 150 (2), and 250 nm (3) from the surface of the implanted stainless steel.

The Fe 2p peak is recorded for two different states: metallic and oxidized ones (Figure 7a), with the oxidized part containing Fe(III) and Fe(II) ions. Three different types of oxidized iron are commonly distinguished: Fe(II) (FeO), a mixture of Fe(II) and Fe(III) ( $\text{Fe}_3\text{O}_4$ ), and Fe(III) (both  $\text{Fe}_2\text{O}_3$  and FeOOH).

The chromium spectrum consists of metallic ( $E_b = 574.5$  eV) and oxidized chromium ( $E_b = 576 \div 576.9$  eV). The latter contains a mixture of Cr(III) oxide and Cr(III) hydroxide (Figure 7). The chromium spectrum includes lines of chromium with the oxidation number Cr(VI) ( $E_b = 579.3$  eV). The authors of reference [65] report on the formation of oxide  $\text{Cr}_2\text{O}_3$  obtained after the implantation of oxygen. This binding energy corresponds to chromates, particularly chromium chromate  $\text{Cr}_2(\text{CrO}_4)_3$ . Apparently, iron chromates are also present in the specimen [31,32]. The peak at  $\sim 577$  eV can correspond to both hydroxide ( $\text{CrOOH}$ ) and oxide ( $\text{Cr}_2\text{O}_3$ ).

It is interesting to note [66] that Cr exists mainly as Cr(III) in the form of various compounds, such as  $\text{Cr}_2\text{O}_3$ ,  $\text{CrCl}$ , and  $\text{Cr}(\text{OH})_3$ . However, it is also found in  $\text{CrO}_3$  and  $\text{Cr}_2\text{O}_7$  compounds.

The iron spectrum consists of lines of pure iron ( $E_b = 706.8$  eV), ferrous oxide  $\text{FeO}$  ( $E_b = 709.8$  eV), and Fe(III) compounds ( $E_b = 710.0 \div 714.0$  eV). Iron, in the oxidized states, predominates on the surface. With depth, the concentration of pure iron begins to prevail. The ratio of  $\text{Fe}^{2+}/\text{Fe}^{3+}$  elements is shown in Table 3.

**Table 3.** XPS analysis of the ratio of the  $\text{Fe}^{3+}/\text{Fe}^{2+}$  peak areas.

Depth, nm	$\text{Fe}^{3+}$ Peak (%)	$\text{Fe}^{2+}$ Peak (%)	Metallic Fe Peak (%)	$\text{Fe}^{2+}/\text{Fe}^{3+}$ Ratio
0 nm	15.06	73.964	10.97	4.9/1
150 nm	23.84	41.76		1.8/1
250 nm	14.76	18.25	48.93	1.3/1

From Table 3, it can be seen that the Fe(II) peak is mostly dominant, but the metallic iron peak becomes the main one at depths more than 250 nm.

The decrease in the concentration of metallic chromium in ion-implanted surface layers is associated with its intense oxidation and the formation of passivating chromium oxide  $\text{Cr}_2\text{O}_3$  after ion treatment (Table 4).

**Table 4.** XPS analysis of the ratio of the  $\text{Cr}^{3+}/\text{Cr}^{6+}$  peak areas.

Depth, nm	$\text{Cr}^{3+}$ Peak (%)	$\text{Cr}^{6+}$ Peak (%)	Metallic Cr Peak (%)	$\text{Cr}^{3+}/\text{Cr}^{6+}$ Ratio
0 nm	91.25094	6.6155	2.133565	13.8/1
150 nm	60.66318	2.807458	36.52937	21.6/1
250 nm	37.82	0	62.17	

The presence of metal oxides, including aluminum oxide, is clearly seen from the oxygen spectrum (Figure 8). A part of the implanted oxygen binds to the substrate elements with the formation of oxides, and a part remains chemically and physically sorbed. Since the Gibbs energy  $\Delta G_f$  of the  $\text{Al}_2\text{O}_3$  formation is lower than that of the formation of Cr and Fe oxides and/or hydroxides [66], the rate of formation of  $\text{Al}_2\text{O}_3$  is higher than that for  $(\text{Cr,Fe})_2\text{O}_3$ . Thus, all of the aluminum is converted into  $\text{Al}_2\text{O}_3$  during implantation, binding the physically and chemically sorbed oxygen. At a depth of 250 nm, oxidized aluminum is not detected, and the concentration of other oxidized metals also decreases. Oxygen reveals another property, i.e., a passivating one. This can be explained by the fact that protective films formed on iron alloys in the presence of oxygen consist not of magnetite ( $\text{Fe}_3\text{O}_4$ ) formed in deaerated media [40,41], but of  $\gamma\text{-Fe}_2\text{O}_3$ , which is called maghemite.

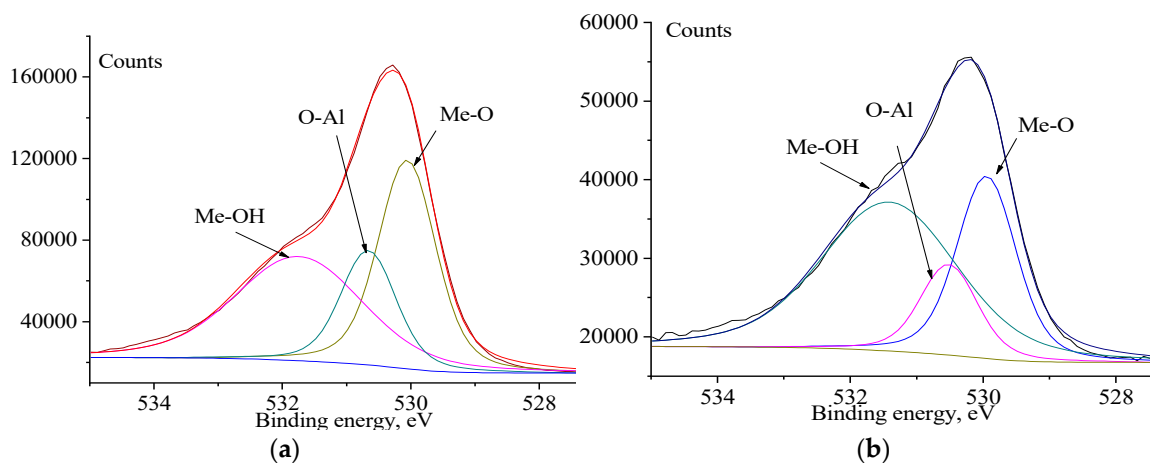


**Figure 8.** XPS spectra of oxygen recorded at depths of 0 (a) and 150 nm (b) from the surface of the implanted stainless steel.

The number of oxidized forms on the surface (Figure 8) is three times higher than at the depth of 150 nm, but the ratio between various oxidized forms (metal oxides—aluminum oxide—metal hydroxides) is almost the same, with the exception of hydroxide forms, which start to increase.

The oxide compounds  $\text{Al}_2\text{O}_3$ ,  $\text{Cr}_2\text{O}_3$ , and  $\text{NiCr}_2\text{O}_4$  (a mixture of  $\text{Cr}_2\text{O}_3$  and NiO) provide strong protection for the specimen against corrosion.

After corrosion tests, the percentage of aluminum oxides in the surface layers of the material changes insignificantly (Table 5), but the ratio between hydroxides and oxides changes in favor of the latter. This is due to the oxidation of all elements of the substrate (Figure 9).

**Table 5.** XPS analysis of oxygen peak ratio.

State	Me-O Peak (%)	Al-O Peak (%)	O-OH Peak (%)
Before corrosion			
0 nm	44.8089	28.02857	27.16253
150 nm	37.88082	27.2717	34.84748
After corrosion			
0 nm	51.92621	30.36293	17.71086
150 nm	44.06879	34.0043	21.92691

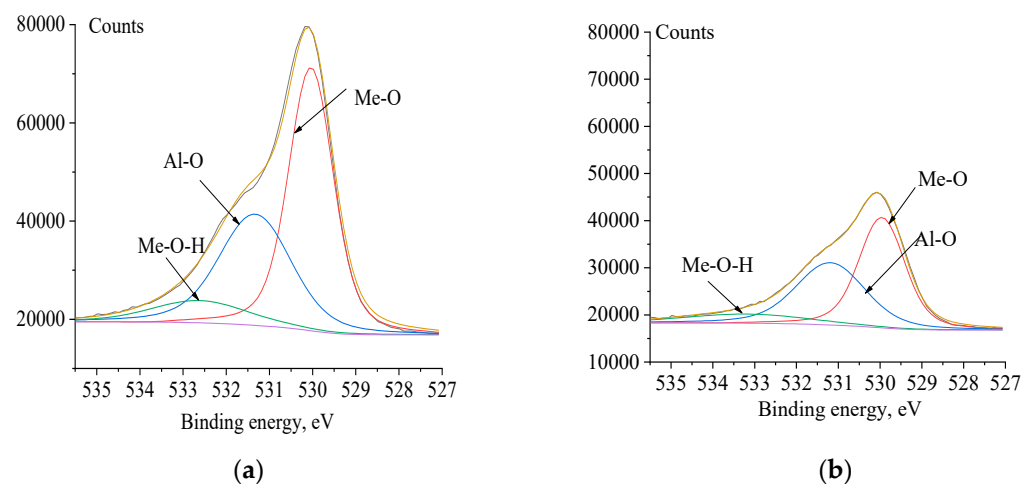


**Figure 9.** XPS spectra of oxygen after corrosion tests at depths of 0 (a) and 150 nm (b).

During boron implantation, boron penetrates into the intergranular space and prevents chromium carbide formation and intergranular corrosion, i.e., it stabilizes the structure of the material [41,67]. At a distance exceeding 25 nm, boron is recorded only at the noise level (Figure 10).

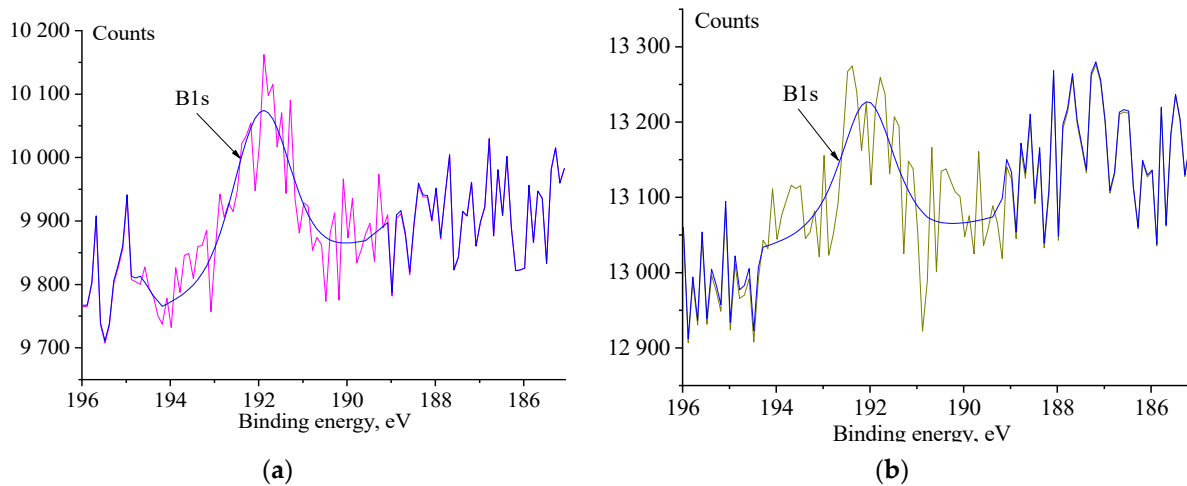


**Figure 10.** XPS spectra of boron recorded at depths of 0 (a) and 25 nm (b) from the surface of the implanted stainless steel.

Boron compounds are not in the surface layers. In addition, the authors found that the presence of oxygen can prevent the formation of borides [67].

It is known that B-containing materials have a smaller amount of the  $\sigma$ -phase and a larger amount of Cr, which diffuses from the matrix to the surface and forms a Cr-rich oxide on the surface, which also contributes to corrosion resistance [67].

#### 4. Conclusions

Oxygen, aluminum, and boron ions were implanted into a stainless steel surface using ion implantation.

The experimental results show that ion implantation improves the corrosion resistance of metal. The non-implanted steel specimen is characterized by severe surface corrosion damage with weight loss (1.5 mg per 800 h). Ion treatment increases the corrosion resistance of stainless steel and changes the nature of its electrochemical corrosion behavior. The higher the concentration of implanted ions and the deeper they penetrate, the higher the corrosion resistance of the resulting material (about 0.2 mg for the first 100 h, then 0 mg). The corrosion rate of the implanted samples decreased approximately 1.8 times in comparison to the non-implanted ones.

According to the XPS data, ion implantation changes the elemental composition of surface layers of the steel specimens and activates a number of chemical reactions, in particular, the intensive formation of aluminum and chromium oxides and nickel–chromium spinels with increased corrosion resistance.

According to the analysis of microdiffraction patterns and XPS analysis, the main phases of implanted samples are the compounds  $\text{Cr}_2\text{O}_3$ , NiO ( $\text{NiCr}_2\text{O}_4$ ).

The insignificant concentration of boron and aluminum in near-surface layers increases the corrosion resistance of the material. Aluminum forms  $\text{Al}_2\text{O}_3$  oxides. Boron does not form compounds and is in free form, which is consistent with the data in the literature.

The determination of the sufficient concentration of the implanted elements in order to increase the corrosion resistance of the material in aggressive media, on the retention of the geometric dimensions of the workpieces and their physical and mechanical properties, is the subject of future research.

Ion implantation can also be performed on carbon steels. When implanting carbon steels, it will be necessary to take into account the lack of a sufficient amount of chromium

and nickel ions for the growth of corrosion-resistant oxides. These ions must be implanted to form a corrosion-resistant barrier layer.

**Author Contributions:** Conceptualization, T.I.D. and M.V.F.; methodology, M.V.F.; validation, V.P.S. and M.V.F.; investigation, T.I.D., O.V.S., T.A.G., A.R.S. and M.V.F.; resources, V.P.S.; writing—original draft preparation, T.I.D.; writing—review and editing, M.V.F., funding acquisition, V.P.S. All authors have read and agreed to the published version of the manuscript.

**Funding:** This research was performed under the government statement of work for ISPMS Project No. FWRW-2021-0003 257.

**Institutional Review Board Statement:** Not applicable.

**Informed Consent Statement:** Not applicable.

**Data Availability Statement:** Not applicable.

**Conflicts of Interest:** The authors declare no conflict of interest.

## References

1. Schweitzer, P.A. *Fundamentals of Corrosion-Mechanisms, Causes, and Preventative Methods*; CRC Press: Boca Raton, FL, USA, 2013; Volume 53, ISBN 9788578110796.
2. Galal, A.; Amin, K.M.; Atta, N.F.; Abd El-Rehim, H.A. Protective Ability of Graphene Prepared by  $\gamma$ -Irradiation and Impregnated with Organic Inhibitor Applied on AISI 316 Stainless Steel. *J. Alloys Compd.* **2017**, *695*, 638–647. [[CrossRef](#)]
3. Gaber, G.A.; Mohamed, L.Z.; Järvenpää, A.; Hamada, A. Enhancement of Corrosion Protection of AISI 201 Austenitic Stainless Steel in Acidic Chloride Solutions by Ce-Doped TiO<sub>2</sub> Coating. *Surf. Coat. Technol.* **2021**, *423*, 127618. [[CrossRef](#)]
4. Dorofeeva, M.S.; Dorofeeva, T.I.; Gritsenko, B.P.; Sergeev, V.P. Thermo-Barrier Nanostructure Microplasma Coatings of ZrO<sub>2</sub>. *J. Phys. Conf. Ser.* **2018**, *1115*, 032067. [[CrossRef](#)]
5. Zhang, X.; Xiao, G.-y.; Jiao, Y.; Zhao, X.-c.; Lu, Y.-p. Facile Preparation of Hopeite Coating on Stainless Steel by Chemical Conversion Method. *Surf. Coat. Technol.* **2014**, *240*, 361–364. [[CrossRef](#)]
6. Sudagar, A.J.; Subasri, R. Fabrication and Characterization of Silver/Nickel Sulphide Solar Absorber Coatings on Stainless Steel by Chemical Bath Deposition. *Mater. Chem. Phys.* **2015**, *163*, 478–484. [[CrossRef](#)]
7. Zhang, X.-m.; Chen, Z.-y.; Li, X.-t.; Ji, K.-p.; Luo, H.-f.; Wan, G.-p.; Yang, S.-f. Influence of Thermal Diffusion Treatment on Microstructure Evolution and Corrosion Behavior of Hot-Dipped Al Coated Fe-Cr-Si-B Cast Steel. *Trans. Nonferrous Met. Soc. China (Engl. Ed.)* **2023**, *33*, 1522–1539. [[CrossRef](#)]
8. Yu, Z.; Chen, M.; Wang, J.; Li, F.; Zhu, S.; Wang, F. Enamel Coating for Protection of the 316 Stainless Steel against Tribo-Corrosion in Molten Zinc Alloy at 460 °C. *J. Mater. Sci. Technol.* **2021**, *65*, 126–136. [[CrossRef](#)]
9. Luo, K.Y.; Jing, X.; Sheng, J.; Sun, G.F.; Yan, Z.; Lu, J.Z. Characterization and Analyses on Micro-Hardness, Residual Stress and Microstructure in Laser Cladding Coating of 316L Stainless Steel Subjected to Massive LSP Treatment. *J. Alloys Compd.* **2016**, *673*, 158–169. [[CrossRef](#)]
10. Ji, X.; Luo, C.; Jin, J.; Zhang, Y.; Sun, Y.; Fu, L. Tribocorrosion Performance of 316L Stainless Steel Enhanced by Laser Clad 2-Layer Coating Using Fe-Based Amorphous Powder. *J. Mater. Res. Technol.* **2022**, *17*, 612–621. [[CrossRef](#)]
11. Saidi, D.; Zaid, B.; Souami, N.; Saoula, N.; Siad, M.; Si Ahmed, A.; Biberian, J.P. AES Depth Profiles in Mo-Coated 304L Stainless Steel Achieved by RF-Magnetron Sputtering and Influence of Mo on the Corrosion in 3.5% NaCl Solution. *J. Alloys Compd.* **2015**, *645*, 45–50. [[CrossRef](#)]
12. Jin, J.; Zhang, J.; Hu, M.; Li, X. Investigation of High Potential Corrosion Protection with Titanium Carbonitride Coating on 316L Stainless Steel Bipolar Plates. *Corros. Sci.* **2021**, *191*, 109757. [[CrossRef](#)]
13. Dorofeeva, T.; Gubaidulina, T.; Sergeev, V.; Fedorischeva, M. Si-Al-N-O Multi-Layer Coatings with Increased Corrosion Resistance Deposited on Stainless Steel by Magnetron Sputtering. *Metals* **2022**, *12*, 254. [[CrossRef](#)]
14. Gubaidulina, T.A.; Dorofeeva, T.I.; Sergeev, V.P.; Kalashnikov, M.P.; Voronov, A.V. The Structure and Composition of Al-Si-N/Ni/Al-Si-N Three-Layer Coatings Deposited by Magnetron Sputtering. In Proceedings of the AIP Conference Proceedings, Tomsk, Russia, 6–10 September 2021; American Institute of Physics Inc.: College Park, MD, USA, 2022; Volume 2509.
15. Paschalidou, E.M.; Shu, R.; Boyd, R.; Papaderakis, A.A.; Bakhit, B.; le Febvrier, A.; Greczynski, G.; Eklund, P.; Nyholm, L. The Effect of the Nb Concentration on the Corrosion Resistance of Nitrogen-Containing Multicomponent TiZrTaNb-Based Films in Acidic Environments. *J. Alloys Compd.* **2022**, *927*, 167005. [[CrossRef](#)]
16. Manivannan, R.; Sundararaj, S.; Dheenasagar, R.; Giridharan, K.; Sivaraman, P.R.; Udhayarani, V. Influence of Al<sub>2</sub>O<sub>3</sub>, SiC and B<sub>4</sub>C Covalent Multilayer PVD Coating on Surface Properties of HSS Rod. *Mater. Today Proc.* **2020**, *39*, 700–707. [[CrossRef](#)]
17. Dorofeeva, T.I.; Gubaidulina, T.A.; Sergeev, V.P.; Kalashnikov, M.P.; Voronov, A.V. Change in the Structure and Corrosion Resistance of a Nickel-Chrome Coating on Stainless Steel During Implantation of High Energy Al<sup>+</sup> and B<sup>+</sup> Ions. *Russ. Phys. J.* **2020**, *63*, 1186–1194. [[CrossRef](#)]

18. Cheon, K.H.; Park, C.; Kang, M.H.; Park, S.; Kim, J.; Jeong, S.H.; Kim, H.E.; Jung, H.D.; Jang, T.S. A Combination Strategy of Functionalized Polymer Coating with Ta Ion Implantation for Multifunctional and Biodegradable Vascular Stents. *J. Magnes. Alloys* **2021**, *9*, 2194–2206. [[CrossRef](#)]
19. Wei, X.; Li, Z.; Liu, P.; Li, S.; Peng, X.; Deng, R.; Zhao, Q. Improvement in Corrosion Resistance and Biocompatibility of AZ31 Magnesium Alloy by NH<sub>2</sub><sup>+</sup> Ions. *J. Alloys Compd.* **2020**, *824*, 153832. [[CrossRef](#)]
20. Dorofeeva, M.S.; Gubaidulina, T.A.; Sergeev, V.P.; Dorofeeva, T.I. Influence of Ion Beam Implantation on the Corrosion Properties of Stainless Steel. In Proceedings of the 2020 7th International Congress on Energy Fluxes and Radiation Effects (EFRE) 2020, Tomsk, Russia, 14–26 September 2020; pp. 766–768. [[CrossRef](#)]
21. Majhi, R.; Rajbhar, M.K.; Das, P.; Elliman, R.G.; Chatterjee, S. Low energy ion beam-induced joining of TiO<sub>2</sub> nanoparticles. *J. Alloys Compd.* **2022**, *924*, 166440. [[CrossRef](#)]
22. Eisen, F.H.; Welch, B. *Ion Implantation*; Elsevier: Amsterdam, The Netherlands, 1971; pp. 1–4. [[CrossRef](#)]
23. Pavlov, P.V.; Zorin, E.I.; Tetelbaum, D.I.; Khokhlov, A.F. Nitrogen as Dopant in Silicon and Germanium. *Phys. Status Solidi* **1976**, *35*, 11–36. [[CrossRef](#)]
24. Pavlov, P.V.; Zorin, E.I.; Tetelbaum, D.I.; Lesnikov, V.P.; Ryzhkov, G.M.; Pavlov, A.V. Phase Transformations at Bombardment of Al and Fe Polycrystalline Films with B<sup>+</sup>, C<sup>+</sup>, N<sup>+</sup>, P<sup>+</sup>, and As<sup>+</sup> Ions. *Phys. Status Solidi* **1973**, *19*, 373–378. [[CrossRef](#)]
25. Langouche, G. Ion Implantation. *Hyperfine Interact.* **1992**, *68*, 95–106. [[CrossRef](#)]
26. Savaloni, H.; Habibi, M. Influence of Ni Deposition and Subsequent N + Ion Implantation at Different Substrate Temperatures on Nano-Structure and Corrosion Behaviour of Type 316 and 304 Stainless Steels. *Appl. Surf. Sci.* **2011**, *258*, 103–112. [[CrossRef](#)]
27. Pedraza, F.; Grosseau-Poussard, J.L.; Dinhut, J.F. Low Energy-High Flux Nitrogen Implantation of an Oxide-Dispersion- Strengthened FeAl Intermetallic Alloy. *Thin Solid Films* **2004**, *467*, 140–145. [[CrossRef](#)]
28. Wang, F.; Zheng, L.; Li, Q.; Zhang, F.; Chen, X.; Zhang, H. Corrosion Properties of Carbon Ions Implanted Chromium Coating Prepared on CSS-42L Aerospace Bearing Steel. *Surf. Coat. Technol.* **2018**, *349*, 392–399. [[CrossRef](#)]
29. Seo, E.J.; Cho, L.; Kim, J.K.; Mola, J.; Zhao, L.; Lee, S.; De Cooman, B.C. Focused Ion Beam-Induced Displacive Phase Transformation from Austenite to Martensite during Fabrication of Quenched and Partitioned Steel Micro-Pillar. *J. Alloys Compd.* **2020**, *812*, 152061. [[CrossRef](#)] [[PubMed](#)]
30. Shi, K.; Zhang, W.; Ning, Z.; Wang, H.; Liao, J.; Yang, Y.; Liu, N.; Yang, J. Microstructural Evolution and Hardening Effect of 12Cr2W2Mn Ferritic/Martensitic Steel under Au-Ions Irradiation. *J. Alloys Compd.* **2020**, *835*, 155360. [[CrossRef](#)]
31. Liu, L.; Wu, Z.; An, X.; Xiao, S.; Cui, S.; Lin, H.; Fu, R.K.Y.; Tian, X.; Wei, R.; Chu, P.K.; et al. *Excellent Adhered Thick Diamond-like Carbon Coatings by Optimizing Hetero-Interfaces with Sequential Highly Energetic Cr and C Ion Treatment*; Elsevier B.V.: Amsterdam, The Netherlands, 2018; Volume 735, ISBN 8675526032.
32. Sergeev, O.V.; Kalashnikov, M.P.; Fedorishcheva, M.V.; Sergeev, V.P.; Panin, V.E. Modification of Ti-Al-N Coatings by High Energy (Cr<sup>+</sup> + B<sup>+</sup>) Ion Bombardment. In Proceedings of the AIP Conference Proceedings, Tomsk, Russia, 19–23 September 2016; Volume 1783. [[CrossRef](#)]
33. Genel, K.; Ozbek, I.; Bindal, C. Kinetics of Boriding of AISI W1 Steel. *Mater. Sci. Eng. A* **2003**, *347*, 311–314. [[CrossRef](#)]
34. Campos, I.; Palomar-Pardavé, M.; Amador, A.; VillaVelázquez, C.; Hadad, J. Corrosion Behavior of Boride Layers Evaluated by the EIS Technique. *Appl. Surf. Sci.* **2007**, *253*, 9061–9066. [[CrossRef](#)]
35. García-León, R.A.; Martínez-Trinidad, J.; Campos-Silva, I.; Figueroa-López, U.; Guevara-Morales, A. Development of Tribological Maps on Borided AISI 316L Stainless Steel under Ball-on-Flat Wet Sliding Conditions. *Tribol. Int.* **2021**, *163*, 107161. [[CrossRef](#)]
36. Klepper, C.C.; Hazelton, R.C.; Yadlowsky, E.J.; Carlson, E.P.; Keitz, M.D.; Williams, J.M.; Zuh, R.A.; Poker, D.B. Amorphous Boron Coatings Produced with Vacuum Arc Deposition Technology. *J. Vac. Sci. Technol. A Vac. Surf. Film.* **2002**, *20*, 725–732. [[CrossRef](#)]
37. Panda, J.N.; Wong, B.C.; Medvedovski, E.; Egberts, P. Enhancement of Tribo-Corrosion Performance of Carbon Steel through Boronizing and BN-Based Coatings. *Tribol. Int.* **2021**, *153*, 106666. [[CrossRef](#)]
38. Rodríguez-Castro, G.; Campos-Silva, I.; Chávez-Gutiérrez, E.; Martínez-Trinidad, J.; Hernández-Sánchez, E.; Torres-Hernández, A. Mechanical Properties of FeB and Fe<sub>2</sub>B Layers Estimated by Berkovich Nanoindentation on Tool Borided Steel. *Surf. Coat. Technol.* **2013**, *215*, 291–299. [[CrossRef](#)]
39. Dellasega, D.; Russo, V.; Pezzoli, A.; Conti, C.; Lecis, N.; Besozzi, E.; Beghi, M.; Bottani, C.E.; Passoni, M. Boron Films Produced by High Energy Pulsed Laser Deposition. *Mater. Des.* **2017**, *134*, 35–43. [[CrossRef](#)]
40. Pelleg, J.; Judelewicz, M. Diffusion in the B $\alpha$ -Fe System and Compound Formation between Electron Gun Deposited Boron Thin Films and Steel Substrate. *Thin Solid Films* **1992**, *215*, 35–41. [[CrossRef](#)]
41. Upadhyay, N.; Pujar, M.G.; Das, C.R.; Krishna, N.G.; Mallika, C.; Kamachi Mudali, U. Pitting Corrosion Behaviour of Boron Added Modified 9Cr–1Mo Steel: Combined Effects of Alkali and Chloride Ions. *Trans. Indian Inst. Met.* **2015**, *68*, 129–141. [[CrossRef](#)]
42. Pogrebnjak, A.D.; Danilionok, M.M.; Uglov, V.V.; Erdybaeva, N.K.; Kirik, G.V.; Dub, S.N.; Rusakov, V.S.; Shypulyenko, A.P.; Zukovski, P.V.; Tuleushev, Y.Z. Nanocomposite Protective Coatings Based on Ti-N-Cr/Ni-Cr-B-Si-Fe, Their Structure and Properties. *Vacuum* **2009**, *83*, 235–239. [[CrossRef](#)]
43. Henriksen, O.; Johnson, E.; Johansen, A.; Sarholt-Kristensen, L.; Wood, J.V. The effect of boron implantation on the corrosion behaviour, microhardness and contact resistance of copper and silver surfaces. *Nucl. Instrum. Methods Phys. Res. Sect. B Beam Interact. Mater. At.* **1987**, *19–20*, 253–258. [[CrossRef](#)]

44. Sourani, F.; Enayati, M.H.; Ashrafizadeh, F.; Sayyed, F.S.; Chu, P.K. Enhancing Surface Properties of (Fe,Cr)Al–Al<sub>2</sub>O<sub>3</sub> Nanocomposite by Oxygen Ion Implantation. *J. Alloys Compd.* **2021**, *853*, 156892. [[CrossRef](#)]
45. Bystrov, S.G.; Reshetnikov, S.M.; Borisova, E.M.; Klimova, I.N.; Kolotov, A.A.; Zhikharev, A.V.; Bayankin, V.Y. Effect of Implantation of Argon and Oxygen Ions on the Physicochemical Properties and Corrosion and Electrochemical Behavior of 14Cr17Ni2 Chromium–Nickel Steel. *Inorg. Mater. Appl. Res.* **2022**, *13*, 666–673. [[CrossRef](#)]
46. Nieh, C.W.; Xiong, F.; Ahn, C.C.; Zhou, Z.; Jamieson, D.N.; Vreeland, T.; Fultz, B.; Tombrello, T.A. Formation of Buried Oxide in MeV Oxygen Implanted Silicon. *MRS Proc.* **1987**, *107*, 73–78. [[CrossRef](#)]
47. Vorobiev, V.L.; Bakieva, O.R.; Gilmudinov, F.Z.; Kolotov, A.A.; Averkiev, I.K.; Borisova, E.M.; Reshetnikov, S.M. Effect of Oxygen Ion Implantation on Physicochemical Structure and Corrosion-Electrochemical Behavior of Copper–Manganese Alloy. *Inorg. Mater. Appl. Res.* **2021**, *12*, 581–587. [[CrossRef](#)]
48. Ren, J.; Yu, L.; Liu, Y.; Ma, Z.; Liu, C.; Li, H.; Wu, J. Corrosion Behavior of an Al Added High-Cr ODS Steel in Supercritical Water at 600 °C. *Appl. Surf. Sci.* **2019**, *480*, 969–978. [[CrossRef](#)]
49. Tang, M.; Wang, J.; Feng, Z.; Li, G.; Yan, Z.; Zhang, R. Corrosion Resistance of AlN and Fe<sub>3</sub>Al Reinforced Fe-Based Plasma Cladding Layer in 3.5 wt% NaCl Solution. *Ceram. Int.* **2019**, *45*, 16918–16926. [[CrossRef](#)]
50. Hamdy, E.; Liu, F.; Geers, C. Superior Protection by  $\alpha$ -Al<sub>2</sub>O<sub>3</sub>/ $\alpha$ -LiAlO<sub>2</sub> Double Oxide Scales against Alkali Carbonate Corrosion. *Corros. Sci.* **2023**, *218*, 111217. [[CrossRef](#)]
51. Gavrilov, N.V.; Kamenetskikh, A.S.; Tretnikov, P.V.; Chukin, A.V. Ion Assisted Deposition of  $\alpha$ -Al<sub>2</sub>O<sub>3</sub> Coatings by Anodic Evaporation in the Arc Discharge. *Surf. Coat. Technol.* **2018**, *337*, 453–460. [[CrossRef](#)]
52. Cordes, S.E. Thermal Stability of  $\gamma$ -Alumina PVD Coatings and Analysis of Their Performance in Machining of Austenitic Stainless Steels. *CIRP J. Manuf. Sci. Technol.* **2012**, *5*, 20–25. [[CrossRef](#)]
53. Xin, Y.C.; Chu, P.K. Plasma Immersion Ion Implantation (PIII) of Light Alloys. In *Surface Engineering of Light Alloys: Aluminium, Magnesium and Titanium Alloys*; Woodhead Publishing: Sawston, UK, 2010; pp. 362–397. [[CrossRef](#)]
54. Sreenivas Rao, K.V.; Tejaswini, G.C.; Girisha, K.G. Corrosion Behavior of Plasma Sprayed Cr<sub>2</sub>O<sub>3</sub>–Al<sub>2</sub>O<sub>3</sub>–ZrO<sub>2</sub> Multilayer Coatings on Mild Steel. *Mater. Today Proc.* **2018**, *5*, 24068–24074. [[CrossRef](#)]
55. Sreenu, A.V. Aluminium-Boron Nitride Nano Composite Coating by Friction Surfacing on Low Carbon Steel Substrate—A Feasibility Study. *Mater. Today Proc.* **2018**, *5*, 26829–26835. [[CrossRef](#)]
56. Zepon, G.; Nascimento, A.R.C.; Kasama, A.H.; Nogueira, R.P.; Kiminami, C.S.; Botta, W.J.; Bolfarini, C. Design of Wear Resistant Boron-Modified Supermartensitic Stainless Steel by Spray Forming Process. *Mater. Des.* **2015**, *83*, 214–223. [[CrossRef](#)]
57. Jiang, J.; Wang, Y.; Zhong, Q.; Zhou, Q.; Zhang, L. Preparation of Fe<sub>2</sub>B Boride Coating on Low-Carbon Steel Surfaces and Its Evaluation of Hardness and Corrosion Resistance. *Surf. Coat. Technol.* **2011**, *206*, 473–478. [[CrossRef](#)]
58. Kuterbekov, K.A.; Nurkenov, S.A.; Kislitsin, S.B.; Kuketayev, T.A.; Tussupbekova, A.K. Investigation of Structure and Properties of Barrier Layers in Metals (Fe, Cu) at Low Temperatures. *Russ. Phys. J.* **2016**, *59*, 978–983. [[CrossRef](#)]
59. Gardin, E.; Zanna, S.; Seyeux, A.; Allion-Maurer, A.; Marcus, P. Comparative Study of the Surface Oxide Films on Lean Duplex and Corresponding Single Phase Stainless Steels by XPS and ToF-SIMS. *Corros. Sci.* **2018**, *143*, 403–413. [[CrossRef](#)]
60. Voyshnis, S.; Seyeux, A.; Zanna, S.; Martin-Cabanas, B.; Couvant, T.; Marcus, P. Oxide Layer Growth on Nickel-Base Alloy Surfaces in High Temperature Water and in O<sub>2</sub> Studied by ToF-SIMS with Isotopic Tracers. *Corros. Sci.* **2018**, *145*, 212–219. [[CrossRef](#)]
61. Lv, Y.; Luo, H.; Tang, J.; Guo, J.; Pi, J.; Ye, K. Corrosion Properties of Phase Reversion Induced Nano/Ultrafine Grained AISI 304 Metastable Austenite Stainless Steel. *Mater. Res. Bull.* **2018**, *107*, 421–429. [[CrossRef](#)]
62. Zhou, M.; Shi, Y.; Yang, J. Denoising Star Map Data via Sparse Representation and Dictionary Learning. *Optik* **2015**, *126*, 1133–1137. [[CrossRef](#)]
63. Wesolowski, D.J.; Ziemniak, S.E.; Anovitz, L.M.; Machesky, M.L.; Bénézech, P.; Palmer, D.A. Solubility and Surface Adsorption Characteristics of Metal Oxides. In *Aqueous Systems at Elevated Temperatures and Pressures: Physical Chemistry in Water, Steam and Hydrothermal Solutions*; Academic Press: Cambridge, MA, USA, 2004; pp. 493–595. [[CrossRef](#)]
64. Peter, R.; Saric, I.; Piltaver, I.K.; Badovinac, I.J.; Petracic, M. Oxide Formation on Chromium Metal Surfaces by Low-Energy Oxygen Implantation at Room Temperature. *Thin Solid Films* **2017**, *636*, 225–231. [[CrossRef](#)]
65. Wang, J.; Cui, Y.; Bai, J.; Dong, N.; Liu, Y.; Zhang, C.; Han, P. Effect of B Addition on the Microstructure and Corrosion Resistance of S31254 Super Austenitic Stainless Steels after Solid Solution Treatment. *Mater. Lett.* **2019**, *252*, 60–63. [[CrossRef](#)]
66. Dorogokupets, P.I.; Sokolova, T.S.; Dymshits, A.M.; Litasov, K.D. Thermodynamic properties of rock-forming oxides,  $\alpha$ -Al<sub>2</sub>O<sub>3</sub>, Cr<sub>2</sub>O<sub>3</sub>,  $\alpha$ -Fe<sub>2</sub>O<sub>3</sub>, and Fe<sub>3</sub>O<sub>4</sub> at high temperatures and pressures. *Geodyn. Tectonophys.* **2016**, *7*, 459–476. [[CrossRef](#)]
67. Avdienko, K.I.; Avdienko, A.A.; Kovalenko, I.A. Effect of the Elemental Composition of an Ion Beam on the Phase Formation and Surface Strengthening of Structural Materials. *Phys. Met. Metallogr.* **2001**, *92*, 623–627.

**Disclaimer/Publisher’s Note:** The statements, opinions and data contained in all publications are solely those of the individual author(s) and contributor(s) and not of MDPI and/or the editor(s). MDPI and/or the editor(s) disclaim responsibility for any injury to people or property resulting from any ideas, methods, instructions or products referred to in the content.